



Space-Time Variability of UTLS Chemical Distribution in the Asian Summer Monsoon Viewed by Limb and Nadir Satellite Sensors

Jiali Luo^{1,2}, Laura L. Pan², Shawn B. Honomichl², John W. Bergman^{2,3}, William J. Randel², Gene Francis², Cathy Clerbaux⁴, Maya George⁴, Xiong Liu⁵, and Wenshou Tian¹

5 ¹Key Laboratory of Semi-Arid Climate Change and College of Atmospheric Sciences, Lanzhou University, Lanzhou, China

²National Center for Atmospheric Research, Boulder, Colorado, USA

³Bay Area Environmental Research Institute, Sonoma, California, USA

⁴LATMOS/IPSL, UPMC Université Paris 06 Sorbonne Université, UVSQ, CNRS, Paris, France

⁵Harvard-Smithsonian Center for Astrophysics, Cambridge, Massachusetts, USA

10 *Correspondence to:* Jiali Luo (luojl@lzu.edu.cn)

Abstract. The Asian Summer Monsoon (ASM) creates a hemispheric scale signature in trace gas distributions in the upper troposphere and lower stratosphere (UTLS). Data from satellite retrievals are the best source of information for characterizing these large-scale signatures. Measurements from the Microwave Limb Sounder (MLS), a limb viewing satellite sensor, have been the most widely used retrieval products for these type of studies. This work explores the information content for the ASM upper troposphere from two nadir-viewing sensors, IASI and OMI. Day-to-day behaviour of carbon monoxide (CO) and ozone (O₃) in the UTLS from these two nadir-viewing sensors are analysed in comparison to MLS to examine the information content for the ASM UTLS trace gas analyses. Day-to-day changes in tracer distributions in response to dynamical variability is explored, to assess whether these nadir viewing sensors provide useful information for investigating sub-seasonal variability. Our result shows that both nadir-viewing instruments capture the impact of ASM dynamics on spatial distribution of tracers in the UTLS. Despite the limited vertical resolution, tropospheric profiles from IASI are able to represent the upper tropospheric enhancement of CO in the region of ASM anticyclone. Similarly, the OMI O₃ profile product is capable of distinguishing the tropospheric dominated air mass in the anticyclone from the stratospheric dominated background on a daily time scale. The high horizontal sampling density of IASI data show finer structures in the horizontal distribution of CO compared to the limb viewing MLS, including CO enhancement in the upper troposphere over the western Pacific resulting from the eastward eddy shedding of the ASM anticyclone. Sub-seasonal variability of tracers is correlated with the dynamical structure of the anticyclone as represented by the geopotential height (GPH) field, and systematic differences between the nadir and limb sounder results are discussed.

1. Introduction

30 As a prominent atmospheric circulation feature in the upper troposphere and lower stratosphere (UTLS) during boreal summer, the Asian Summer Monsoon (ASM) anticyclone has been investigated widely in recent years (Hoskins and Rodwell, 1995;



Highwood and Hoskins, 1998; Zhang et al., 2002; Liu et al., 2007; Wu et al., 2015). It is bounded by the westerly jet to the north, easterly jet to the south, and noted for prolonged air confinement (Dunkerton, 1995). Due to the influences of deep convection and air confinement, seasonal-mean chemical compositions within the anticyclone near the tropopause display distinctly surface-like characteristics; boundary layer and tropospheric tracers, such as CO, H₂O, HCN, and a large set of hydrocarbons, are significantly enhanced while O₃ as a stratospheric tracer is significantly decreased (Park et al., 2004; Li et al., 2005; Randel and Park, 2006; Park et al., 2007; Randel et al., 2010; Vernier et al., 2011; Garny and Randel, 2013).

Although the ASM anticyclone is a strong and steady feature of seasonal scale circulations in UTLS, it undergoes variations on sub-seasonal timescales. These include 10-20 day westward migrations and the associated eddy shedding (Hsu and Plumb, 2000; Popovic and Plumb, 2001). Previous studies have shown that the monsoon circulation has active/break cycles that are linked to oscillations of deep convection with timescales of 10-20 and 30-60 days (i.e., Krishnamurti and Bhalme, 1976; Krishnamurti and Ardanuy, 1980; Annamalai and Slingo, 2001; Randel and Park, 2006). Zhang et al. (2002) found that the center of the anticyclone shows bimodality in its longitude location that they classify in terms the Tibetan mode (TM, centered at about 90°E) and the Iranian mode (IM, centered at about 60°E), although the degree of bimodality appears dependent on the meteorological dataset (Nützel et al., 2016). A number of recent studies have shown that sub-seasonal scale dynamical processes in the Asian summer monsoon region may play a significant role in UTLS transport of trace gases (Yan et al., 2011; Garny and Randel, 2015; Pan et al., 2016). It is evident that diagnosing intra-seasonal variability of chemical tracers in the UTLS and their interactions with dynamical fields is important for a more complete understanding of the ASM anticyclone's chemical impacts.

Satellite observations provide an essential source of information in ASM UTLS-related studies. Data from limb viewing sensors, the Aura Microwave Limb Sounder (MLS), and the Atmospheric Chemistry Experiment Fourier Transform Spectrometer (ACE-FTS), in particular, are two widely used datasets (e.g., Park et al., 2007; Randel et al., 2010). These Limb sounders offer relatively high vertical resolution but have limited horizontal sampling on daily timescales. Nadir-viewing instruments, on the other hand, offer better horizontal sampling but have limited vertical resolution and are designed primarily to determine column abundances.

This study aims to examine the representation of chemical variability in the ASM UTLS from nadir-viewing sensors. Two specific datasets we explore are CO from the Infrared Atmospheric Sounding Interferometer (IASI) and O₃ from the Ozone Monitoring Instrument (OMI). CO is a pollution tracer and an effective tracer of transport in the troposphere and lower stratosphere (e.g., Bowman, 2006) since it has a photochemical lifetime of 2–3 months (Xiao et al., 2007). O₃ is an effective transport tracer in the UTLS because of the large gradient in its mixing ratio across the tropopause and its long lifetime relative to transport time scales. In the UTLS, O₃ mostly serves as a stratospheric tracer although it also has tropospheric pollution sources. Short time variations of O₃ in the UTLS are largely linked to synoptic scale weather disturbances in the troposphere (Heggin et al., 2008). These two satellite datasets will be examined, together with the MLS CO and O₃, and with meteorological analyses from the Global Forecasting System (GFS) to address the following questions: 1) Do these nadir view instruments, designed primarily for retrieving trace gas column abundance, have sufficient information to show the ASM



dynamics driven trace gas distributions and variability at the UTLS levels? 2) Are the data from nadir sensors consistent with the limb-viewing data on sub-seasonal scales with respect to dynamical variability of tracers in the ASM region? 3) What can we learn from the complementary information from limb and nadir viewing instruments?

Although the IASI CO and OMI O₃ are compared with MLS CO and O₃, respectively, it is not the goal of this work to evaluate the quantitative agreement between the nadir and limb sensors. The difference in viewing geometries make limb-viewing and nadir-viewing datasets fundamentally different quantities because of the different air masses they are sensing. Previous validation studies have shown quantitative comparisons of these two types of data including quantitative comparisons in the UTLS (i.e., Livesey et al., 2008; George et al., 2009; Liu et al., 2010a, 2010b; Kroon et al., 2011; Wachter et al., 2012; Bak et al., 2013; Safieddine et al., 2016; Barret et al., 2016; Huang et al., submitted). In this work, the comparisons are made to evaluate whether data from the two types of sensors provide a consistent picture of the ASM dynamical impact on the UTLS tracer distributions and variabilities. The comparisons will also help to assess the information of the nadir viewing datasets for ASM UTLS studies, and whether they complement the information provided by the much widely used limb sensors, especially in representing the UTLS chemical tracers variability associated with the sub-seasonal oscillation of the ASM anticyclone. From the remote sensing information content point of view, the analysis we present also aim to provide a perspective of whether the high density in horizontal sampling supplement the relatively weak vertical information content when used to inform the dynamical variability of the upper troposphere.

2. Data Description

2.1 Satellite data

For limb-viewing observations, we use MLS Version 4, level 2, 147 hPa CO and 100 hPa O₃ data. MLS is a forward-looking sounder on board the Aura satellite launched in July 2004 (Waters et al., 2006). The vertical resolution of CO retrievals at 147 hPa is 5.1 km and the precision is ~15 ppbv with a systematic uncertainty of ~30 ppbv. The O₃ retrieval has a vertical resolution of 3 km at 100 hPa. The precision and accuracy are ~30 ppbv and ~50 ppbv, respectively (Livesey et al., 2015). As a limb sounder, MLS's field of view produces a horizontal resolution of ~6 km across the track and ~300 km along the track, and has a relatively low daily sampling density (~240 limb scans per orbit with ~3500 profiles during both day and night). In order to make the daily output easier to interpret, daily maps are made by interpolating the output onto a regular grid.

Nadir-viewing observations of CO are obtained from IASI (level 2 data) aboard EUMETSAT's Metop satellite. IASI measures the 'thermal infrared' (TIR) spectrum emitted by the Earth-atmosphere system with twice daily near-global coverage (with 4 simultaneous pixels of 12 km diameter every 50 km), but limited vertical resolution (Clerbaux et al., 2009). The CO tropospheric abundance product is derived from the spectra using FORLI retrieval algorithm using a single a priori profile and covariance matrix (Hurtmans et al., 2012; George et al., 2015). The IASI CO retrieval, however, contains 0.8 to 2.4 (1.5 to 2.0 at mid-latitudes) 'independent pieces of information' (or degrees of freedom signal DOFS; George et al. 2009). This information content allows IASI CO retrieval to capture upper tropospheric variability at mid-latitude and tropical latitudes,



which is supported by in situ measurements from MOZAIC project (correlations ~ 0.7 ; Wachter et al., 2012), satellite observations from the MOPITT instrument (George et al., 2015). IASI data have been shown to reproduce monthly mean large-scale features in the UTLS over the ASM region from GEOS-Chem (a chemical transport model coupled to meteorological analysis from the Goddard Earth Observing System GEOS-5; Barret et al., 2016).

5 Nadir-viewing observations of O_3 are obtained from OMI, an O_3 sounder aboard the Aura satellite that provides daily global coverage at 13 km x 24 km footprint (Levelt et al., 2006). OMI O_3 products include retrievals of both total O_3 columns and vertical profiles. In this study, we use the O_3 profile product by Liu et al. (2010b) and Huang et al. (2016). O_3 profiles are retrieved at 24 vertical layers covering the surface to ~ 60 km using the optimal estimation technique constrained by a monthly and zonal mean O_3 profile climatology (McPeters et al., 2007). NCEP reanalysis tropopause pressure is used to separate the stratosphere from the troposphere. To speed up the processing, the product is produced at a nadir spatial resolution of 52 km x 10 48 km by combining 4 pixels along the track. The retrievals have ~ 6.0 - 7.0 degrees of freedom (5.0-6.7 in the stratosphere; Liu et al., 2005; Liu et al., 2010b; Liu et al., 2010a). Although the vertical resolution of OMI O_3 retrievals in the troposphere is about 10 km (Liu et al., 2010b), the profile product has been shown to have significant and useful information in the UTLS transition region due to the large O_3 gradient across the tropopause and good stratospheric information content (Pittman et al., 15 2009; Liu et al., 2010a; Liu et al., 2010b; Bak et al., 2013). In this work, we use a level-3 product gridded to 1° longitude x 1° latitude horizontal resolution. OMI has known cross-track dependent biases (Liu et al., 2010a; Liu et al., 2010b). Thus, we smoothed O_3 profiles by adjacent data which view zenith angles (VZA) is greater than 58° .

Note that the CO and O_3 data examined in this work are from different years. The CO data are from June-July-August (JJA) of 2012. 2012 was a standard year for IASI with no change in the L2 temperature data (which might induce jumps in the data series). The O_3 are from JJA 2008, the season before the OMI instrument “row anomaly” in January 2009 which impacted the O_3 data quality since then (Huang et al., 2016; Huang, submitted). Since the O_3 and CO are examined separately and the work focuses on daily to sub-seasonal scale space-time variabilities, the choice of different years does not impact the analyses and the conclusions.

To highlight the horizontal sampling density and vertical sensitivity differences between the limb viewing and nadir viewing 25 sensors, Figure 1 shows the geolocations of all IASI and MLS profiles and the representative averaging kernels for the ASM region from a single day (June 1, 2012). It is apparent from Fig. 1a that the horizontal coverage of IASI is much better than MLS. This disparity of sampling density and its implications for representing synoptic scale variability motivates our use of nadir viewing data to characterize chemical distributions in the UTLS on daily to sub-seasonal time scales. Figure 1b shows a vertical information distribution comparison between IASI and MLS CO retrievals. For the interest of this analyses, the IASI 30 vertical information distribution is shown by averaging kernels representing partial columns 12-16 km and 0-12 km, respectively, and is an average of all profiles in the ASM region ($30^\circ E$ - $140^\circ E$ longitudes and $15^\circ N$ - $35^\circ N$ latitudes) for a single day 1 June 2012. MLS is shown by the standard averaging kernel for the 147 hPa product (see MLS version 4.2x level 2 data quality description document, https://mls.jpl.nasa.gov/data/v4-2_data_quality_document.pdf). The figure provides a perspective that IASI retrieval information content is optimized for the middle troposphere. The UT information



is much weaker and influenced by a broad layer ~ 8 km. In contrast, MLS information shows a strong maximum near 14 km (~ 150 hPa) with a vertical distribution ~ 6 km (full-width at half maximum). This figure highlights the differences specific to questions of interest in this work. For more complete averaging kernel discussions, see the work of George et al. (2009) for IASI data and Liu et al. (2010b) for OMI data.

5 2.2 Meteorological analysis data

We use wind fields, geopotential height (GPH), tropopause height, and potential temperature (derived from temperature and pressure) from the Global Forecast System (GFS) operational analysis (a product of the National Centers for Environmental Prediction; NCEP) to diagnose the dynamical variability of ASM anticyclone. These 6-hourly data have a horizontal resolution of 1° on 26 pressure levels (from 1000 hPa to 10 hPa) (National Centers for Environmental Prediction/National Weather Service/NOAA/U.S. Department of Commerce, 2000).

3. Comparisons of MLS, IASI and OMI Data

Previous studies have shown that, during the monsoon season (June-July-August, JJA), the seasonal mean ASM anticyclone has a pronounced chemical signature with enhanced (diminished) mixing ratios of tropospheric (stratospheric) tracers such as CO (O_3) (Randel and Park, 2006; Park et al., 2007; Park et al., 2008; Randel et al., 2010; Pan et al., 2016). To help identify tracers' space-time variability in relation to the anticyclone from the selected satellite data sources, we first assess the ability of the nadir-viewing dataset in representing the well-demonstrated large-scale features of chemical distributions associated with the ASM anticyclone in UTLS on seasonal scales. Vertical ranges of the data were chosen to optimize the overlap of information from nadir and limb viewing instruments with the vertical extent of the anticyclone. Based on the analyses of the dynamical field and trajectory calculations, the chemical confinement in the anticyclone occurs in the pressure range 200-100 hPa or 12-16 km (Randel and Park, 2006). Moreover, the strongest closed circulation of the anticyclone occurs at ~ 15 km, above the main convective outflow level (~ 12 km) (Park et al., 2008). Based on this structure and the vertical information content of IASI CO retrieval (George et al., 2009), we choose to use IASI CO mixing ratios averaged over the altitude range 12-16 km and the MLS CO retrieval from 147 hPa. For O_3 , we use OMI data layer 18 (approximately 100 hPa) and MLS 100 hPa product. A single year of 2008 is selected for O_3 analysis and 2012 for CO analysis.

Figure 2 shows seasonal averages for (a) MLS CO at 147 hPa, (b) IASI CO at 12-16 km, (c) MLS O_3 at 100 hPa and (d) OMI O_3 in layer 18 during the active period of the ASM (JJA). To indicate the seasonal mean location of the anticyclone, Fig. 2 also includes selected GPH contours and wind vectors at 150 hPa (panels a and b) and 100 hPa (panels c and d) from the same period. The chemical signature of the seasonally averaged ASM anticyclone is evident for all quantities. Both MLS and IASI CO data show enhancements within the anticyclone, although IASI has lower values than MLS. Since the largest retrieval sensitivity of IASI CO is in the middle troposphere (~ 500 hPa), the clear CO enhancement in the 12-16 km layer in the



anticyclone indicates that, despite the relatively weak upper tropospheric sensitivity, the IASI data are capable of showing the impact of the ASM circulation on upper tropospheric CO.

Similarly, MLS and OMI data are very consistent in their representations of O₃ distributions at 100 hPa, showing the lower O₃ mixing ratios within the anticyclone, despite the significantly different sampling geometry and vertical resolutions. Note that this chemical structure at 100 hPa level is strongly tied the ASM regional structure of the tropopause (Bian et al., 2012; Pan et al., 2016). Due to the higher tropopause associated with the anticyclone, air within in the anticyclone at 100 hPa is dominated by tropospheric influences, leading to lower O₃ mixing ratios compared to the stratosphere-influenced air outside the anticyclone. The consistency between the two O₃ datasets on seasonal scales indicates that the OMI O₃ profile product is capable of representing the ASM UTLS transition region.

To further quantify the consistency of limb and nadir sounding data in representing the variability, we compare co-located bin averages from IASI CO to MLS (Fig. 3a) as well as OMI O₃ to MLS (Fig. 3b) in the monsoon region (0-50°N, 0-150°E) during JJA. These scatterplots show that variations from nadir viewing instruments are generally consistent with those from MLS. IASI and MLS CO are well correlated ($r = 0.72$; Fig. 3a) although the IASI layer averages have a smaller range of variability than MLS (represented by the small slope of the linear fit, 0.40), likely influenced by using a single a priori profile in CO retrieval (George et al., 2015) and a weaker detection sensitivity in the upper troposphere. The O₃ correlation between OMI and MLS at 100 hPa is stronger ($r = 0.93$); here too, the nadir instrument has somewhat weaker variability (slope = 0.85).

Overall these comparisons show that the nadir viewing data has sufficient sensitivity to capture the UTLS chemical impact by ASM anticyclone. The IASI CO and OMI O₃ products, on the seasonal and ASM regional scale, provide consistent picture with MLS data which has been widely used to investigate chemical tracer distributions and transport in this region (Li et al., 2005; Park et al., 2007; Barret et al., 2008; Livesey et al., 2008; Liu et al., 2013; Huang et al., 2016; Yan et al., 2016). Encouraged by the consistency shown by these correlations, we now proceed to analyze the sub-seasonal scale variability.

4. Sub-seasonal variability of chemical tracers in the ASM UTLS

On seasonal time scales, the ASM anticyclone is a stationary circulation. However, analysis reveals the existence of substantial wave propagation on smaller scales; in particular, 10-20 day east-west oscillation is evident in dynamical fields and model simulated tropospheric tracers (Popovic and Plumb, 2001; Garny and Randel, 2013; Pan et al., 2016). One of the goals in this work is to examine daily spatial structures and variations of tracer fields from the three satellite datasets as they relate to dynamical fields.

Because of the large differences in horizontal sampling density, the limb and nadir data are mapped differently. The daily representation from MLS data requires interpolation to increase the density in coverage, while the IASI and OMI data densities are reduced by binned averages. We explored three interpolation algorithms for mapping MLS CO and O₃ to approximately 5° × 5° latitude-longitude grid. All three methods (cosine smoothing, natural neighbor, inverse distance) are similar, conceptually, in filling the empty cell with weighted mean of nearby observations, but the weightings are determined differently. The



differences produced by these methods do not impact the conclusions of this study. Figure 4 shows maps of retrieved data only (Fig. 4a) and the interpolated data (Fig. 4b), using one day of MLS CO at 147 hPa. Both maps exhibit the co-locations of enhanced CO and high GPH, showing the consistency of the CO enhancement with the large scale dynamical fields that highlight the location of the anticyclone. The small scale structure produced by the mapping should not be over interpreted.

5 4.1. UT CO analysis using MLS and IASI data

We begin our examination of daily maps in Fig. 5, which shows mixing ratios of MLS CO at 147 hPa and the dynamical fields (winds and GPH) at 150 hPa for selected days. During the time period, the dynamical evolution of the anticyclone, as indicated by the selected GPH contours, shows different phases of the east-west oscillation (Pan et al., 2016; Zhang et al., 2002). In this sequence, the anticyclone was initially in the Tibetan mode (Aug 18, center of the anticyclone was located near the southern edge of the Tibetan Plateau) and migrated westward toward the Iranian mode (Aug 20, center of the anticyclone located west of 70 °E). It then continued to elongate and migrate further west (Aug 24), eventually the center splits and the anticyclone was in a double center phase (Aug 26). The spatial distribution of the CO enhancement during this period indicates a similar evolution, following a region of relatively high CO as it migrates together with the center of the anticyclone. Although its horizontal resolution is limited, MLS successfully captures the day to day co-variability of CO with the dynamical fields. This migration of the anticyclone center was also found in terms of potential vorticity (Garny and Randel, 2013) and model simulated CO (Pan et al., 2016).

The IASI 12-16 km CO maps during the same period are shown in Fig. 6. The sequence of maps shows that the daily UT CO enhancement over the ASM region are well detected by IASI retrievals, and the spatial distributions are generally co-located with the anticyclone as represented by the 150 hPa GPH field. Compared to the MLS, the spatial distribution shows many additional finer scale structures (note the color scales in Figs. 5 and 6 are different). On the Aug 18 and 20, IASI 12-16 km CO are much more extended in longitudinal range compared to the MLS, co-located and mimic the east-west extent of the anticyclone. The distributions Aug 24 and 26, in contrast, show clear double centered structure in CO enhancement that are not as well co-located with the 150 hPa GPH distribution. In addition, the IASI CO field shows evidence of eastward shedding over the western Pacific, which subsequently migrates southward following the anticyclonic flow. Additional CO enhancement features appear on the south of the anticyclone migrating toward southwest following the cross-equator flow. It is not clear if this feature originated from the shedding of anticyclone trapped UT air or if it is from an additional boundary layer source. Note that physically there is no reason to expect a perfect correlation between the CO maximum and the GPH maximum, since the dynamical field and the CO mixing ratios are controlled by different processes (Garny and Randel, 2013). A significant correlation at the 150 hPa reflects the strong air mass confinement by the anticyclone and persistent boundary layer emission and localized convective pumping. The interesting differences between the UT CO enhancement locations and the anticyclone center suggest that the IASI 12-16 km retrievals in these cases may have contributions from CO concentrations from below 12 km, which is consistent with the general shape of the averaging kernels (Fig. 1b).



Figure 6 indicates that, despite the limited vertical resolution, IASI contains sufficient information to detect UT CO enhancement. To further examine the consistency of the IASI CO profile vertical structure with the circulation in the monsoon region, Fig. 7 shows a pressure-latitude cross-section of IASI CO for a single day during the monsoon season at 90 °E (where CO is persistently high). Enhanced CO exists throughout the middle and upper troposphere between 20 °N and 30 °N, with a plume of CO that extends from the surface to the tropopause near 20 °N. While the limited vertical resolution of IASI no doubt smoothes the distribution of CO, it is important that IASI is able to detect the signature of upward transport of CO associated with the region of strong vertical winds over Northern India and the southern flank of the Tibetan Plateau. Overall, the vertical structure of the CO enhancement is consistent with the flow field, i.e., the UT CO enhancement is co-located with deep ascending branch of the monsoon Hadley cell (Wang, 2006). For more discussion on the climatological flow structure in the meridional plane, see analyses in Zhang et al. (2002).

To characterize the sub-seasonal variability represented by MLS and IASI CO, Fig. 8 displays Hovmöller diagrams of daily anomaly fields for 150 hPa GPH, 147 hPa MLS CO, and 12-16 km IASI CO in the ASM region (15-35 °N, 0-150 °E) during JJA 2012. We examine the zonal propagation of anomalies and compare the migration of dynamical and chemical features from different datasets throughout the season. GPH anomalies (Fig. 8a) migrate across the region approximately every 10-20 days. MLS CO anomalies also show westward migration but with amplitudes and timing that differ from GPH. However, the westward migration is less regular and limited to east of 30 °E for IASI CO anomalies, although they do exhibit the persistent positive anomaly between 60-90 °E that is common to all three quantities. Interestingly, IASI CO anomalies show eastward migrating features between 120 ° and 150 °E, as shown in Fig. 6. This type of eastward shedding event was seen in the model analysis, following the western Pacific mode of the anticyclone (Pan et al., 2016). We speculate that the weaker westward migration signal and clear eastward migration in the IASI anomaly is contributed by the retrieval information in the level lower than that represented by 150 hPa dynamical field.

The similarity between the two satellite data sets becomes more apparent using regional averages. Figure 9 compares time series of spatial means for the region between the Iranian and Tibetan modes (60-90 °E, 15-35 °N; corresponding to the 60-90 °E average of variability in Fig. 8). In this context, MLS and IASI CO are highly correlated with each other ($r = 0.8$), fluctuating in tandem over the entire season. The association between GPH and the satellite data is less clear. However, they all exhibit similar oscillations during the second half of August and there are better correlations between GPH and CO during July and August, when the ASM is most active, than during June.

In summary, both IASI and MLS CO at the upper troposphere show that the chemical distribution over the region is strongly impacted by the sub-seasonal scale east-west oscillation of the ASM anticyclone. MLS CO and IASI CO agree on regional mean fluctuations despite the fact that the two sensors are influenced by different over vertical columns. The sub-seasonal variability exhibited in the CO data during the Asian Summer Monsoon is broadly consistent with atmospheric model output (Pan et al., 2016). MLS and IASI data have different advantages. MLS data are better for examining features with a shallow vertical extent such as the ASM anticyclone provided those features have a large enough horizontal scale. IASI CO data have a higher horizontal resolution and are able to detect the impacts of vertical transport in the troposphere. The spatial distribution



of IASI CO in UTLS shows additional finer scale structures than MLS and the eastward shedding over the western Pacific is evident in IASI CO field.

4.2. UTLS O₃ analysis using MLS and OMI data

We now turn our attention to the sub-seasonal variations of UTLS O₃ from MLS and OMI. While CO is a boundary layer pollution tracer, O₃ in the UTLS region is foremost a transport tracer highlighting the influence of the stratosphere. Here, the influence of monsoon convection on the UTLS O₃ distribution is somewhat indirect. The large scale O₃ distribution reflects the tropospheric influence on the air mass inside the anticyclone in contrast to the stratospheric influence outside. The structure of the bulging tropopause in the monsoon region (Bian et al., 2012; Pan et al., 2016) is a significant influence of the O₃ distribution (indicated by the interception of the tropopause with the 105 hPa pressure level in Figs. 10&11). Lower O₃ mixing ratios are expected inside the anticyclone in the layer near 100 hPa since the tropopause is at a lower pressure inside the anticyclone than it is outside in this region. Previous work analyzing MLS 100 hPa CO had led to a similar conclusion (Fig. 9, Park et al., 2007).

Figures 10 and 11 examine daily snap shots of O₃ mixing ratios during July 2008. In addition to the GPH field, we also included the tropopause information in the figures. MLS (Fig. 10) exhibits the characteristic low O₃ mixing ratio inside the anticyclone as well as four distinct distributions that are indicative of the east-west oscillation of the ASM anticyclone: the eastern phase with the O₃ minimum centered between 60 ° and 90 °E on July 16 (Fig. 10a), the western phase on Jul 19 (Fig. 10b), the elongated phase on Jul 20 (Fig. 10c), and a double-centered phase on Jul 23 (Fig. 10d). The distribution of O₃ from OMI also shows similar distribution of low O₃ inside the anticyclone but the O₃ inside the anticyclone is significantly lower than the MLS. Quantitatively, OMI data show a sharper transition of O₃ field across the edge of the anticyclone (as indicated by the 105 hPa tropopause contour) and lower O₃ in the anticyclone. The differences between MLS and OMI are more pronounced at low latitudes (i.e., south of 40 °N), where OMI data show finer scale structures.

The Hovmöller diagrams in Fig. 12 examine sub-seasonal variations using the anomaly fields during JJA season of 2008, isolating east-west variations in the dynamical field (in terms of GPH; Fig. 12a) and facilitating comparisons with O₃ variability (Figs. 12b, c). All three anomaly fields are dominated by the persistent location of the anticyclone, leading to positive anomalies of GPH and negative anomalies of O₃ mixing ratios between 30 °E and 120 °E and all three exhibit westward propagating anomalies that traverse that same longitude range. However, those migrations occur with different frequencies; westward migrating GPH anomalies recur every 10 to 20 days, the migrations of MLS O₃ (Fig. 12b) occur perhaps once per month, and westward migrations of OMI O₃ (Fig. 12c) occur with approximately the same frequency as GPH but with smaller amplitudes. There are differences between MLS and OMI in small-scale structures, which clearly reflect the differences in their sampling densities.

As with the analysis of CO data, the comparisons of the time series of spatial averages of O₃ (60-90 °E, 15-35 °N; Fig. 13) is revealing. There is a stronger correspondence between MLS O₃ and GPH ($r = 0.7$) than that with OMI O₃ and GPH ($r = 0.5$).



The correlation between the MLS and OMI sectional anomalies time series is relatively weak ($r = 0.4$). The very different vertical and horizontal samplings of two satellites are likely the reason for the relatively weak correlation.

5. Conclusions

We have examined space-time variability of chemical tracers in the UTLS associated with the ASM represented by nadir viewing (IASI and OMI) satellite instruments in comparison with a widely used limb viewing (MLS) dataset. Using CO (a pollution tracer) and O₃ (a stratospheric tracer), we focus on the strengths and limitations of these data for representing the distribution and variability of UTLS chemical tracers in the region of the dynamically variable ASM anticyclone.

Our analysis shows that the IASI and OMI data provide consistent pictures with MLS data on the overall distributions of CO and O₃ in UTLS over the ASM region. The nadir viewing satellite sensors find enhanced CO and weakened O₃ within the ASM anticyclone, a signature of convective transport (e.g., Park et al., 2004; Li et al., 2005; Randel and Park 2006; Randel et al., 2010; Vernier et al., 2011; Garny and Randel, 2013). IASI CO in 12-16 km layer shows a smaller range of variability compared to 147 hPa MLS CO product, likely due to the weaker UT sensitivity and the use of a single a priori globally in retrieval (George et al., 2009; 2015).

The satellite data analysis highlights the significant role of ASM dynamic variability in controlling the UTLS tracer distribution, and CO often follows the complex evolution of the anticyclone between different modes, supporting and extending the conclusion of previous studies (e.g. Yan et al., 2011; Garney and Randel 2013; Pan et al., 2016). Selected daily maps and Hovmöller diagrams of CO and O₃ in the UTLS region during the ASM from all three datasets illustrate the tracer behavior associated with the east-west oscillation of the anticyclone and eddy shedding events. Although MLS data has a relatively coarse horizontal resolution at daily timescales, the sub-seasonal variations of CO at 147 hPa and O₃ at 100 hPa are consistent with dynamical fields (CO maxima and O₃ minima that are co-located with GPH maxima). The Hovmöller diagrams also reveal westward migration of positive CO and GPH anomalies initiated from the Tibetan Plateau, often with a 10-20 day time scale.

The correspondence between GPH and tracer concentrations from the nadir viewing instruments is also evident. The upper tropospheric CO enhancement in IASI data displays finer scale structures in daily maps, and shows additional transport of CO enhanced air over the western Pacific and spreading equatorward following the anticyclonic flow. This behavior is expected from eastward eddy shedding from the anticyclone, but it has only a weak signature in 150 hPa MLS CO anomalies. Similarly, OMI O₃ daily maps and Hovmöller diagrams show finer structures that are consistent with the ASM dynamical variability.

We also examined the vertical distribution of CO from IASI combined with wind field information. High values of UT CO are consistent with upward motion in the flow field near the southern edge of the Tibetan Plateau as part of the convective-driven ascending branch of the monsoon Hadley cell. In contrast, the regions of relatively low values of CO at high latitudes in the troposphere are consistent with descending air. These results suggest that IASI CO data have sufficient information content to resolve the impact of the ASM circulation and may add information to the vertical CO structure in the region. An analysis using



IASI O₃ retrieval indicates a similar conclusion (Safieddine et al., 2016). This last result, in particular, highlights the benefit of the combined analysis of satellite data from multiple viewing geometries.

Overall, our analysis demonstrates the value of high horizontal sampling density from the nadir viewing sensors in capturing the dynamical variability of UTLS tracer distributions. Although the retrieval has fewer degrees of freedom for each profile, the large number of profiles retrieved daily at finer footprints produces significant information content regarding horizontal dynamic variability. From this analysis, we not only gain confidence in the robustness of features in the ASM chemical structure, but also gain insight into possible retrieval improvement for the nadir sensors. The differences provide clues to understanding more subtle aspects of the retrieval information content of each dataset as well as the interaction of dynamics and chemical distribution in the ASM region.

Statement. The authors declare that they have no conflict of interest.

Acknowledgments. This work is in part J Luo's PhD research, funded by the National Science Foundation of China (41630421 and 41575038). The work is in part conducted at the National Center for Atmospheric Research, operated by the University Corporation for Atmospheric Research under sponsorship of the United State National Science Foundation. The IASI mission is a joint mission of EUMETSAT and the Centre National d'Etudes Spatiales (CNES, France). We thank the ULB team (Daniel Hurtmans, Pierre Coheur) for the development of the FORLI-CO retrieval algorithm, and Mijeong Park for discussion and helpful comments .

References

Annamalai, H., and Slingo, J. M.: Active/break cycles: diagnosis of the intraseasonal variability of the Asian Summer Monsoon, *Climate Dynamics*, 18, 85-102, 2001.

Bak, J., Liu, X., Wei, J. C., Pan, L. L., Chance, K., and Kim, J. H.: Improvement of OMI ozone profile retrievals in the upper troposphere and lower stratosphere by the use of a tropopause-based ozone profile climatology, *Atmos. Meas. Tech.*, 6, 2239-2254, 10.5194/amt-6-2239-2013, 2013.

Barret, B., Ricaud, P., Mari, C., Atti é J. L., Bousserez, N., Josse, B., N, E. L. F., Livesey, N. J., Massart, S., and Peuch, V. H.: Transport pathways of CO in the African upper troposphere during the monsoon season: a study based upon the assimilation of spaceborne observations, *Atmospheric Chemistry & Physics Discussions*, 8, 3231-3246, 2008.

Barret, B., Sauvage, B., Bennouna, Y., and Flochmoen, E. L.: Upper-tropospheric CO and O₃ budget during the Asian summer monsoon, *Atmospheric Chemistry & Physics*, 16, 1-40, 2016.

Bian, J., Pan, L. L., Paulik, L., Vömel, H., Chen, H., and Lu, D.: In situ water vapor and ozone measurements in Lhasa and Kunming during the Asian summer monsoon, *Geophysical Research Letters*, 39, 19808, 2012.

Bowman, K. P.: Transport of carbon monoxide from the tropics to the extratropics, *Journal of Geophysical Research Atmospheres*, 111, 109-125, 2006.



- Clerbaux, C., Boynard, A., Clarisse, L., George, M., Hadji-Lazaro, J., Herbin, H., Hurtmans, D., Pommier, M., Razavi, A., and Turquety, S.: Monitoring of atmospheric composition using the thermal infrared IASI/MetOp sounder, *Atmospheric Chemistry & Physics*, 9, 724-725 passim, 2009.
- Dunkerton, T. J.: Evidence of meridional motion in the summer lower stratosphere adjacent to monsoon regions, *Journal of Geophysical Research Atmospheres*, 100, 16675-16688, 1995.
- 5 Garny, H., and Randel, W. J.: Dynamic variability of the Asian monsoon anticyclone observed in potential vorticity and correlations with tracer distributions, *Journal of Geophysical Research-atmospheres*, 118, 13421-13433, 2013.
- Garny, H., and Randel, W. J.: Transport pathways from the Asian monsoon anticyclone to the stratosphere, *Atmospheric Chemistry & Physics*, 15, 25981-26023, 2015.
- 10 George, M., Clerbaux, C., Hurtmans, D., Turquety, S., Coheur, P. F., Pommier, M., Hadjilazaro, J., Edwards, D. P., Worden, H., and Luo, M.: Carbon monoxide distributions from the IASI/METOP mission: evaluation with other space-borne remote sensors, *Atmospheric Chemistry & Physics*, 9, 9793-9822, 2009.
- George, M., Clerbaux, C., Bouarar, I., Coheur, P. F., Deeter, M. N., Edwards, D. P., Francis, G., Gille, J. C., Hadjilazaro, J., and Hurtmans, D.: An examination of the long-term CO records from MOPITT and IASI: comparison of retrieval
15 methodology, *Bmc Medical Genetics*, 8, 4095-4135, 2015.
- Hegglin, M. I., Boone, C., Manney, G., Shepherd, T. G., Walker, K., Bernath, P., Daffer, W., Hoor, P., and Schiller, C.: Validation of ACE-FTS satellite data in the upper troposphere/lower stratosphere (UTLS) using non-coincident measurements, *Atmospheric chemistry and physics*, 8, 1483-1499, 2008.
- Highwood, E., and Hoskins, B.: The tropical tropopause, *Quarterly Journal of the Royal Meteorological Society*, 124,
20 1579-1604, 1998.
- Hoskins, B. J., and Rodwell, M. J.: A model of the Asian summer monsoon. Part I: The global scale, *Journal of the Atmospheric Sciences*, 52, 1329-1340, 1995.
- Hsu, C. J., and Plumb, R. A.: Nonaxisymmetric Thermally Driven Circulations and Upper-Tropospheric Monsoon Dynamics, *Journal of the Atmospheric Sciences*, 57, 1255-1276, 2000.
- 25 Huang, G., Liu, X., Chance, K., Yang, K., Bhartia, P. K., Cai, Z., Allaart, M., Calpini, B., Coetzee, G., and Cuevas-Agulló E.: Validation of 10-year SAO OMI Ozone Profile (PROFOZ) Product Using Ozone-sonde Observations, *Atmospheric Measurement Techniques Discussions*, (under Review), 2017.
- Huang, L., Jiang, J. H., Murray, L. T., Damon, M. R., Su, H., and Livesey, N. J.: Evaluation of UTLS carbon monoxide simulations in GMI and GEOS-Chem chemical transport models using Aura MLS observations, *Atmospheric Chemistry &
30 Physics*, 16, 5641-5663, 2016.
- Hurtmans, D., Coheur, P. F., Wespes, C., Clarisse, L., Scharf, O., Clerbaux, C., Hadji-Lazaro, J., George, M., and Turquety, S.: FORLI radiative transfer and retrieval code for IASI, *Journal of Quantitative Spectroscopy & Radiative Transfer*, 113, 1391-1408, 2012.
- Krishnamurti, T. N., and Bhalme, H.: Oscillations of a monsoon system. Part I. Observational aspects, *Journal of the*



- Atmospheric Sciences, 33, 1937-1954, 1976.
- Krishnamurti, T. N., and Ardanuy, P.: The 10 to 20 - day westward propagating mode and “Breaks in the Monsoons”, *Tellus*, 32, 15-26, 1980.
- Kroon, M., de Haan, J. F., Veeffkind, J. P., Froidevaux, L., Wang, R., Kivi, R., and Hakkarainen, J. J.: Validation of operational ozone profiles from the ozone monitoring instrument, *Journal of Geophysical Research*, 116, 2011.
- Levelt, P. F., Van, d. O., G. H. J, Dobber, M. R., and Malkki, A.: The ozone monitoring instrument, *IEEE Transactions on Geoscience & Remote Sensing*, 44, 1093-1101, 2006.
- Li, Q., Jiang, J. H., Wu, D. L., Read, W. G., Livesey, N. J., Waters, J. W., Zhang, Y., Wang, B., Filipiak, M. J., and Davis, C. P.: Trapping of Asian pollution by the Tibetan anticyclone: A global CTM simulation compared with EOS MLS observations, *Geophys. Res. Lett.*, 32, L14826, 2005.
- Liu, J., Logan, J., Murray, L. T., Pumphrey, H., Schwartz, M., and Megretskaia, I.: Transport analysis and source attribution of seasonal and interannual variability of CO in the tropical upper troposphere and lower stratosphere, *Atmospheric Chemistry and Physics*, 13, 129, 2013.
- Liu, X., Chance, K., Sioris, C., Spurr, R., Kurosu, T., Martin, R., and Newchurch, M.: Ozone profile and tropospheric ozone retrievals from the Global Ozone Monitoring Experiment: Algorithm description and validation, *Journal of Geophysical Research: Atmospheres*, 110, 2005.
- Liu, X., Bhartia, P., Chance, K., Froidevaux, L., Spurr, R., and Kurosu, T.: Validation of Ozone Monitoring Instrument (OMI) ozone profiles and stratospheric ozone columns with Microwave Limb Sounder (MLS) measurements, *Atmospheric Chemistry and Physics*, 10, 2539-2549, 2010a.
- Liu, X., Bhartia, P. K., Chance, K., Spurr, R. J. D., and Kurosu, T. P.: Ozone profile retrievals from the Ozone Monitoring Instrument, *Atmos. Chem. Phys.*, 10, 2521-2537, [10.5194/acp-10-2521-2010](https://doi.org/10.5194/acp-10-2521-2010), 2010b.
- Liu, Y., Hoskins, B., and Blackburn, M.: Impact of Tibetan orography and heating on the summer flow over Asia, *Journal of the Meteorological Society of Japan. Ser. II*, 85, 1-19, 2007.
- Livesey, N., Filipiak, M., Froidevaux, L., Read, W., Lambert, A., Santee, M., Jiang, J., Pumphrey, H., Waters, J., and Cofield, R.: Validation of Aura Microwave Limb Sounder O₃ and CO observations in the upper troposphere and lower stratosphere, *Journal of Geophysical Research: Atmospheres*, 113, 2008.
- Livesey, N. J., Read, W. G., Wagner, P. A., Froidevaux, L., Lambert, A., Manney, G. L., Millán Valle, L. F., Pumphrey, H. C., Santee, M. L., Schwartz, M. J., Wang, S., Fuller, R. A., Jarnot, R. F., Knosp, B. W., and Martinez, E.: Version 4.2 level 2 data quality and description document, 2015.
- McPeters, R. D., Labow, G. J., and Logan, J. A.: Ozone climatological profiles for satellite retrieval algorithms, *Journal of Geophysical Research: Atmospheres*, 112, 2007.
- National Centers for Environmental Prediction/National Weather Service/NOAA/U.S. Department of Commerce: NCEP FNL operational model global tropospheric analyses continuing from July 1999. [Available at [10.5065/D6M043C6](https://doi.org/10.5065/D6M043C6) Research Data Archive at the National Center for Atmospheric Research, Computational and Information Systems Laboratory, Boulder,



- Colo.], 2000.
- Nützel, M., Dameris, M., and Garny, H.: Movement, drivers and bimodality of the South Asian High, *Atmospheric Chemistry and Physics*, 16, 14755-14774, 2016.
- Pan, L. L., Honomichl, S. B., Kinnison, D. E., Abalos, M., Randel, W. J., Bergman, J. W., and Bian, J.: Transport of chemical tracers from the boundary layer to stratosphere associated with the dynamics of the Asian summer monsoon, *Journal of Geophysical Research: Atmospheres*, 121, 2016.
- 5 Park, M., Randel, W. J., Kinnison, D. E., Garcia, R. R., and Choi, W.: Seasonal variation of methane, water vapor, and nitrogen oxides near the tropopause: Satellite observations and model simulations, *Journal of Geophysical Research: Atmospheres*, 109, 2004.
- 10 Park, M., Randel, W. J., Gettelman, A., Massie, S. T., and Jiang, J. H.: Transport above the Asian summer monsoon anticyclone inferred from Aura Microwave Limb Sounder tracers, *Journal of Geophysical Research: Atmospheres*, 112, 2007.
- Park, M., Randel, W. J., Emmons, L. K., Bernath, P. F., Walker, K. A., and Boone, C. D.: Chemical isolation in the Asian monsoon anticyclone observed in Atmospheric Chemistry Experiment (ACE-FTS) data, *Atmospheric Chemistry and Physics*, 8, 757-764, 2008.
- 15 Pittman, J. V., Pan, L. L., Wei, J. C., Irion, F. W., Liu, X., Maddy, E. S., Barnet, C. D., Chance, K., and Gao, R. S.: Evaluation of AIRS, IASI, and OMI ozone profile retrievals in the extratropical tropopause region using in situ aircraft measurements, *Journal of Geophysical Research: Atmospheres*, 114, 2009.
- Popovic, J. M., and Plumb, R. A.: Eddy shedding from the upper-tropospheric Asian monsoon anticyclone, *Journal of the atmospheric sciences*, 58, 93-104, 2001.
- 20 Randel, W. J., and Park, M.: Deep convective influence on the Asian summer monsoon anticyclone and associated tracer variability observed with Atmospheric Infrared Sounder (AIRS), *Journal of Geophysical Research: Atmospheres*, 111, 2006.
- Randel, W. J., Park, M., Emmons, L., Kinnison, D., Bernath, P., Walker, K. A., Boone, C., and Pumphrey, H.: Asian monsoon transport of pollution to the stratosphere, *Science*, 328, 611-613, 2010.
- 25 Safieddine, S., Boynard, A., Hao, N., Huang, F., Wang, L., Ji, D., Barret, B., Ghude, S. D., Coheur, P.-F., and Hurtmans, D.: Tropospheric ozone variability during the East Asian summer monsoon as observed by satellite (IASI), aircraft (MOZAIC) and ground stations, *Atmospheric Chemistry and Physics*, 16, 10489-10500, 2016.
- Vernier, J. P., Thomason, L., and Kar, J.: CALIPSO detection of an Asian tropopause aerosol layer, *Geophysical Research Letters*, 38, 2011.
- 30 Wachter, E. D., Barret, B., Flochmoň, E. L., Pavelin, E., Matricardi, M., Clerbaux, C., Hadji-Lazaro, J., George, M., Hurtmans, D., Coheur, P.-F., Nedelec, P., and Cammas, J. P.: Retrieval of MetOp-A/IASI CO profiles and validation with MOZAIC data, *Atmospheric Measurement Techniques*, 5, 2843-2857, 2012.
- Wang, B.: *The asian monsoon*, Springer Science & Business Media, 2006.
- Waters, J. W., Froidevaux, L., Harwood, R. S., Jarnot, R. F., Pickett, H. M., Read, W. G., Siegel, P. H., Cofield, R. E., Filipiak,



- 5 M. J., Flower, D. A., Holden, J. R., Lau, G. K., Livesey, N. J., Manney, G. L., Pumphrey, H. C., Santee, M. L., Wu, D. L., Cuddy, D. T., Lay, R. R., Loo, M. S., Perun, V. S., Schwartz, M. J., Stek, P. C., Thurstans, R. P., Boyles, M. A., Chandra, K. M., Chavez, M. C., Chen, G. S., Chudasama, B. V., Dodge, R., Fuller, R. A., Girard, M. A., Jiang, J. H., Jiang, Y., Knosp, B. W., Labelle, R. C., Lam, J. C., Lee, A. K., Miller, D., Oswald, J. E., Patel, N. C., Pukala, D. M., Quintero, O., Scaff, D. M., Vansnyder, W., Tope, M. C., Wagner, P. A., and Walch, M. J.: The earth observing system microwave limb sounder (EOS MLS) on the Aura satellite, *IEEE Transactions on Geoscience and Remote Sensing*, 44, 1075-1092, 2006.
- Watson, D. F., *Contouring: A Guide to the Analysis and Display of Spatial Data*, Pergamon Press, ISBN 008040286 0, 1992.
- Wu, G., He, B., Liu, Y., Bao, Q., and Ren, R.: Location and variation of the summertime upper-troposphere temperature maximum over South Asia, *Climate Dynamics*, 45, 2757-2774, 2015.
- 10 Xiao, Y., Jacob, D. J., and Turquety, S.: Atmospheric acetylene and its relationship with CO as an indicator of air mass age, *Journal of Geophysical Research: Atmospheres*, 112, 2007.
- Yan, R., Bian, J., and Fan, Q.: The Impact of the South Asia High Bimodality on the Chemical Composition of the Upper Troposphere and Lower Stratosphere, *Atmospheric and Oceanic Science Letters*, 4, 229–234, 2011.
- Yan, X., Wright, J. S., Zheng, X., Livesey, N. J., Vömel, H., and Zhou, X.: Validation of Aura MLS retrievals of temperature, water vapour and ozone in the upper troposphere and lower-middle stratosphere over the Tibetan Plateau during boreal summer, 9, 3547-3566, 2016.
- 15 Zhang, Q., Guoxiong, W., and Yongfu, Q.: The bimodality of the 100 hPa South Asia High and its relationship to the climate anomaly over East Asia in summer, *Journal of the Meteorological Society of Japan. Ser. II*, 80, 733-744, 2002.

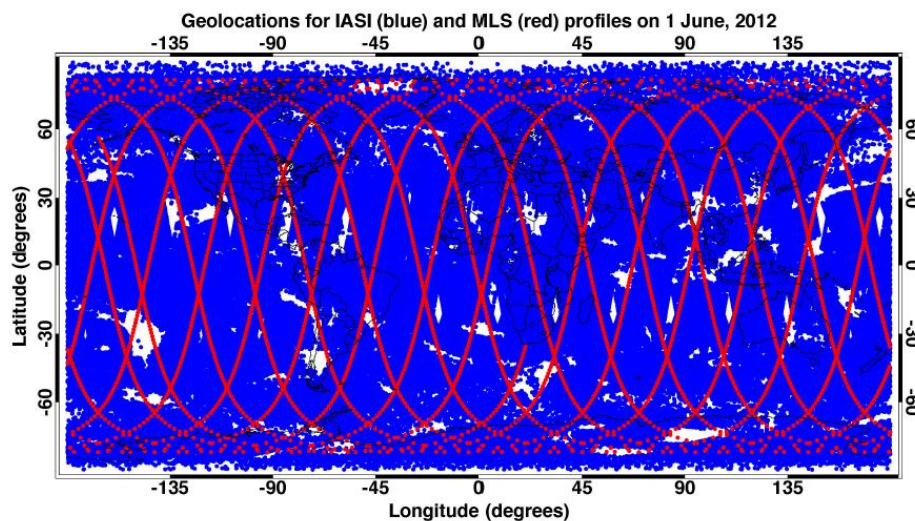


Figure 1a: Retrieval geolocations for the nadir viewing instrument IASI (blue) and the limb viewing instrument MLS (red) with enlarged symbols on June 1, 2012. Both day and night observations are included.

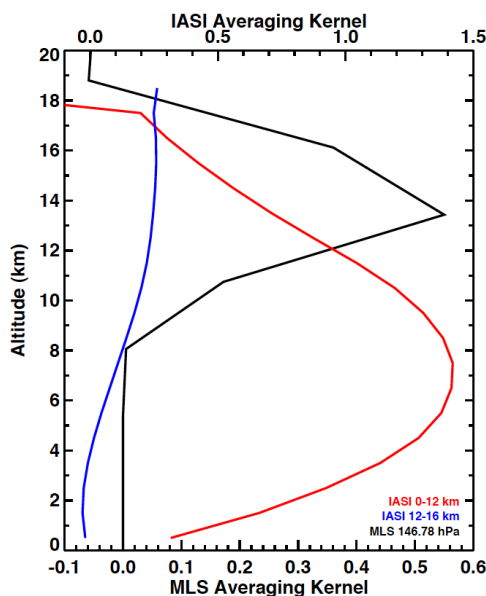


Figure 1b: IASI averaging kernels for partial columns 0-12 km (in red) and 12-16 km (in blue). MLS averaging kernel for the 146.78 hPa product (in black). The curves represent the average of all profiles from 30 °E-140 °E longitudes and 15 °N-35 °N latitudes on June 1st 2012.

5

10

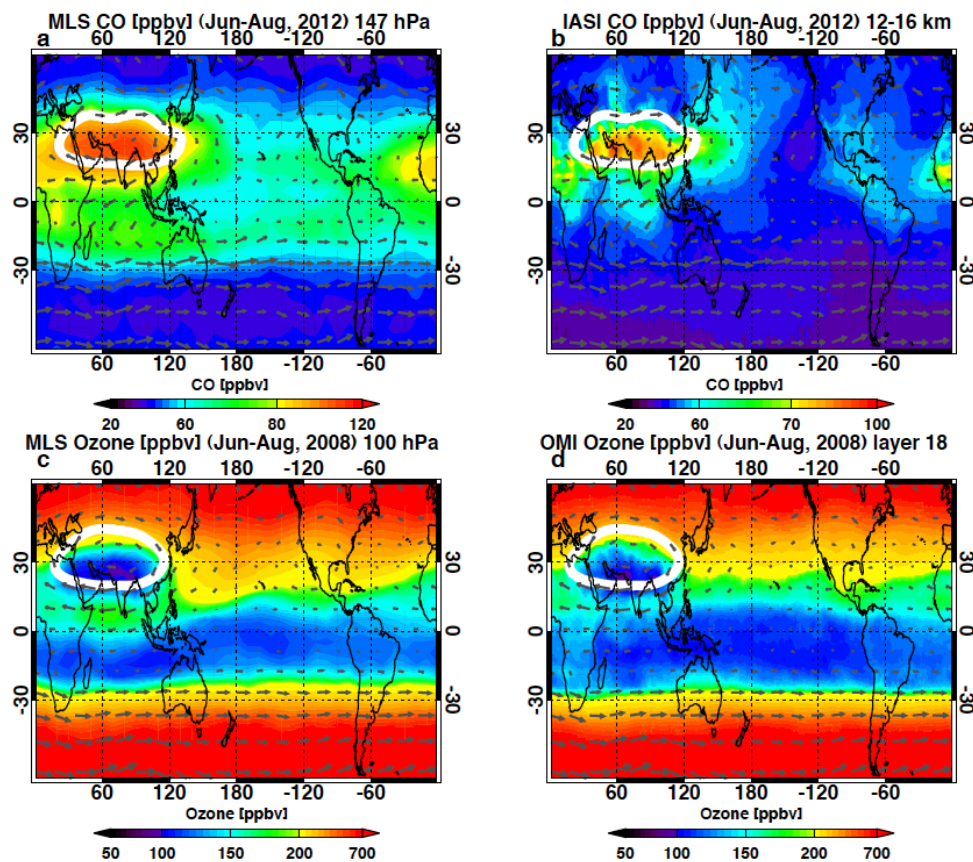


Figure 2: Horizontal distributions of June-August mean of CO mixing ratio for (a) MLS at 147 hPa, (b) IASI in the 12-16 km layer for 2012, and O₃ for (c) MLS and (d) OMI at 100 hPa for 2008. The GFS horizontal wind vectors are over plotted using gray arrows. The boundary of the ASM anticyclone is displayed in panels (c) and (d) using the 16.7 km geopotential height (GPH) contour at 100 hPa and in panels (a) and (b) using the 14.3 km contour at 150 hPa (white contour). Note the color scales for IASI and MLS CO are different. MLS data has been averaged over 5°(lat) × 10°(lon) bins; IASI and OMI are 2° × 3° averages.

5

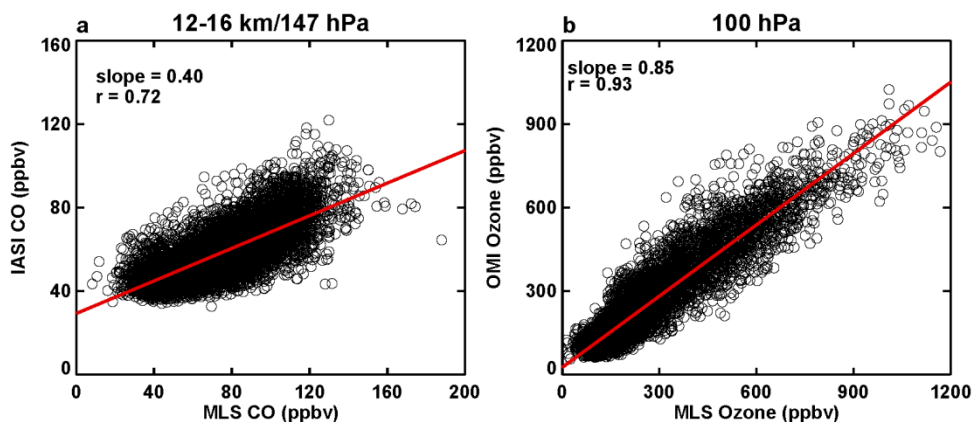


Figure 3: (a) Scatterplot of IASI 12-16 km average CO mixing ratio versus MLS CO at 147 hPa for June, July, and August (JJA) 2012. (b) Scatterplot of OMI and MLS 100 hPa O₃ for JJA 2008. Values are averaged daily over 6° by 10° latitude-longitude boxes from Asian summer monsoon region (0-50°N, 0-150°E). Correlations and slopes for the linear fit are shown in the upper left corner of each panel.

5

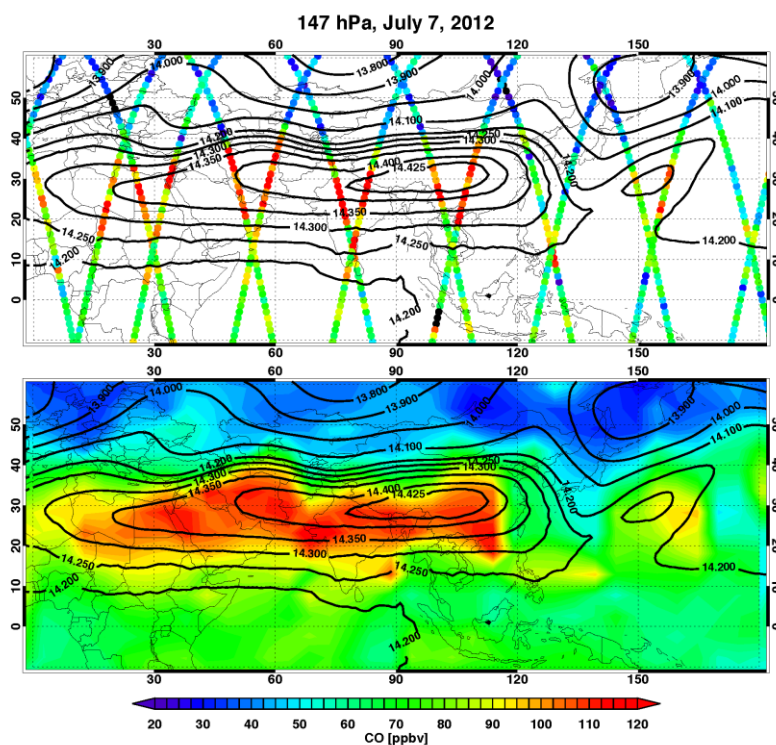


Figure 4: MLS 147 hPa CO mixing ratio at retrieval geolocation on July 7, 2012 (top) and the interpolated map using the natural neighbor algorithm (Watson, 1992). Black contours show selected GPH of 150 hPa.

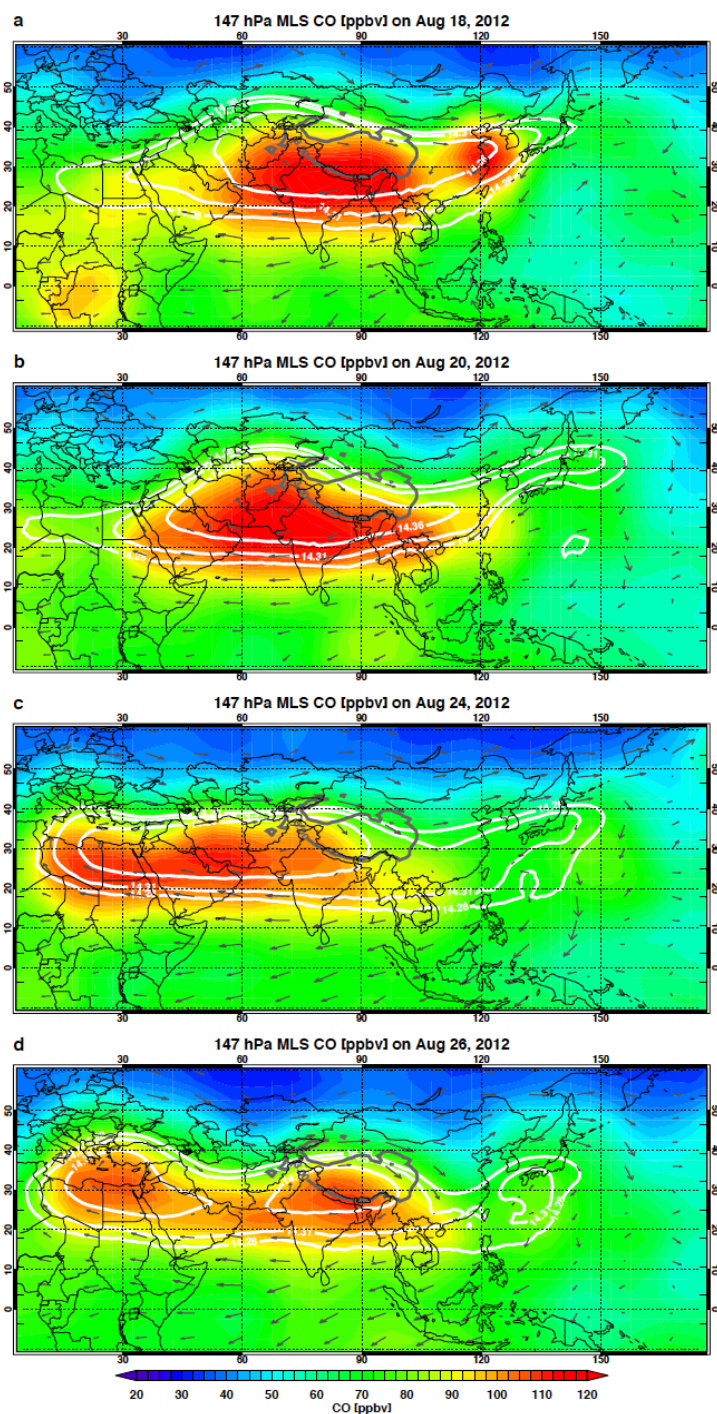


Figure 5: Daily maps of MLS CO mixing ratio at 147 hPa (color shading) on (a) Aug 18, (b) Aug 20, (c) Aug 24, and (d) Aug 26, 2012. The thick gray lines are the 600 hPa contour of surface pressure, indicating the location of the Tibetan Plateau (TP). Horizontal wind vectors are over plotted as gray arrows. The location of the anticyclone is outlined in white by 150 hPa GPH contours for 14.28, 14.31, and 14.36 km. MLS data are mapped using cosine smoothing in $5^\circ \times 5^\circ$ latitude-longitude bins.

5

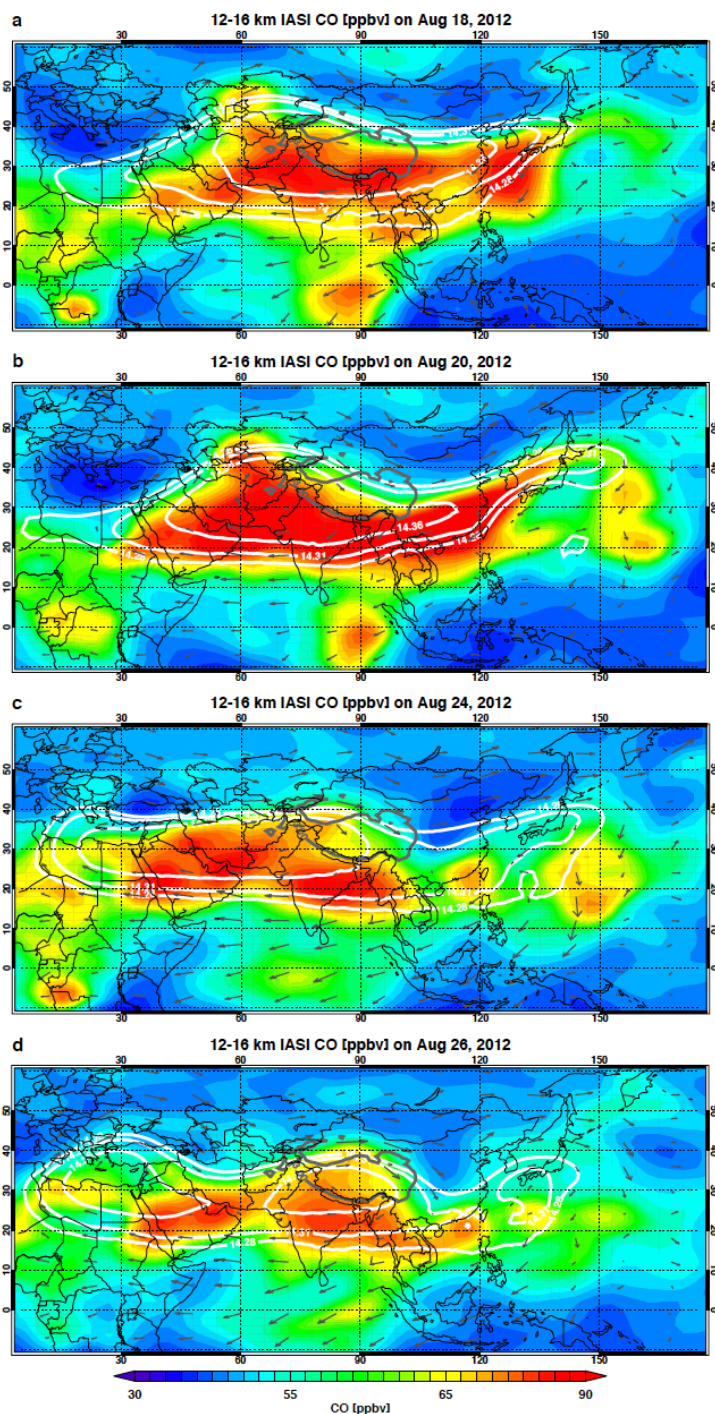


Figure 6: Same as Fig. 5, but for IASI CO 12-16 km layer average mixing ratio. IASI data are mapped in $2^\circ \times 3^\circ$ latitude \times longitude grids. A Gaussian smoothing is used to fill missing data points.

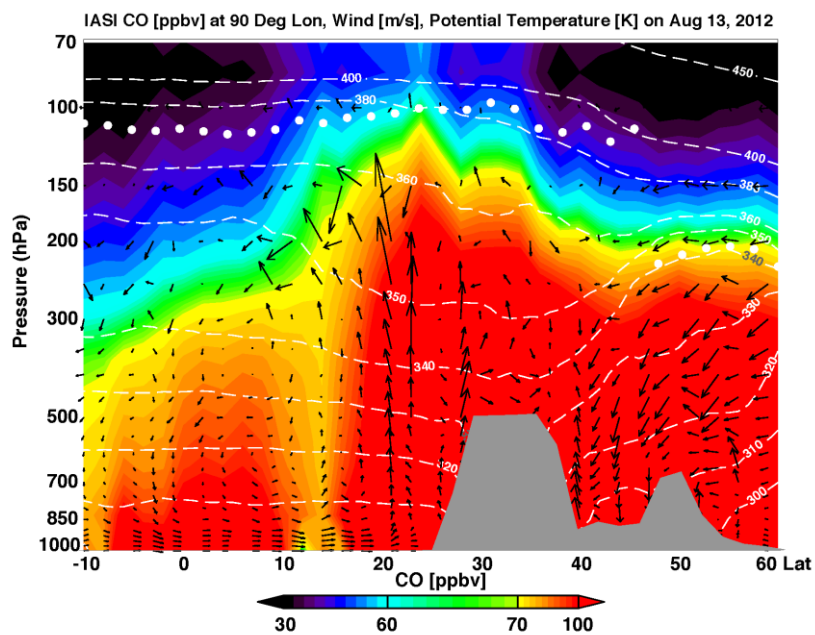


Figure 7: A pressure-latitude cross section of IASI CO mixing ratios (color shading) along 90°E on Aug 13, 2012. Also shown are selected potential temperature levels (white dash), the tropopause height (white dots), the wind field (black vectors) and the shape of the terrain top (Gray shaded).

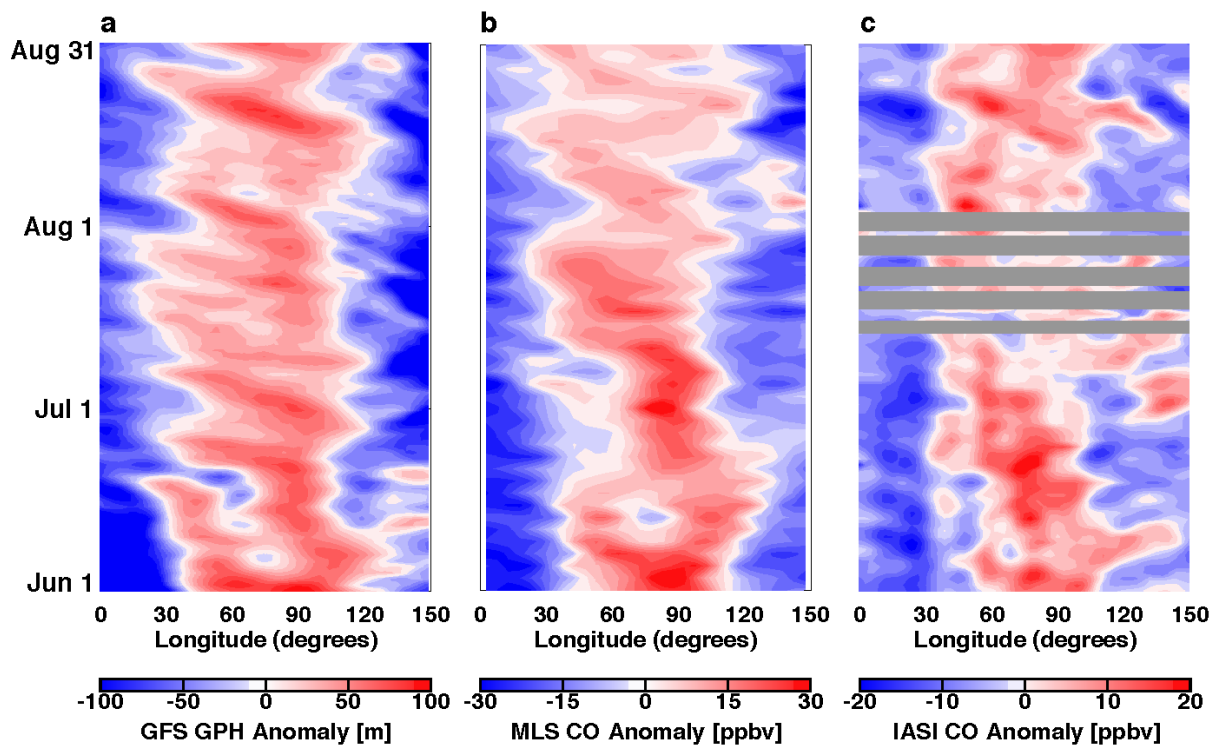


Figure 8: Longitudinal-time (Hovmoller) diagrams for (a) 150 hPa geopotential height (GPH) anomalies, (b) MLS CO anomalies at 147 hPa, and (c) IASI CO anomalies at 12-16 km for 2012. Anomalies are calculated with respect to the regional mean (15-35 °N, 0-150 °E), MLS values have been averaged over 5 °bins, and IASI data have been averaged over 3 °bins. Anomalies are calculated from daily averages. Time period with missing data are marked in gray.

5

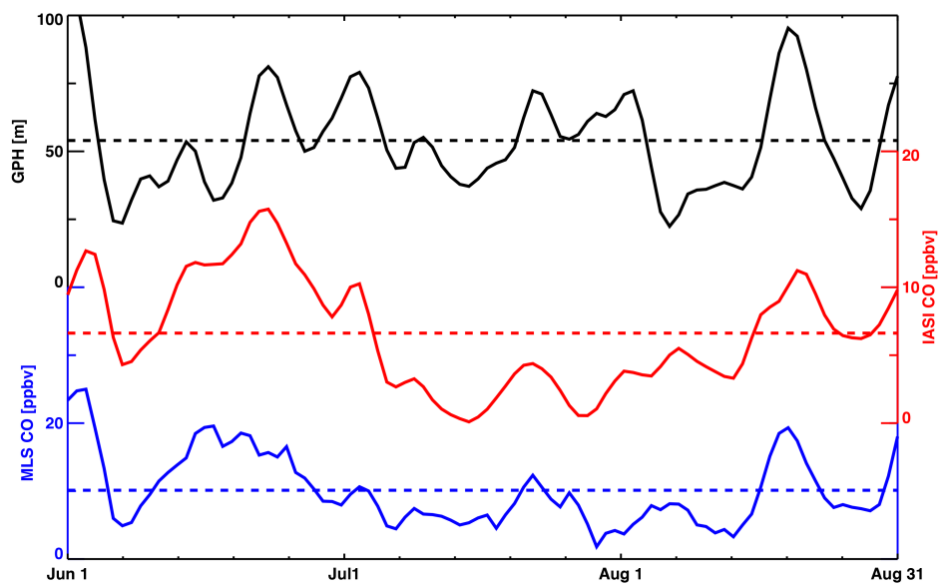
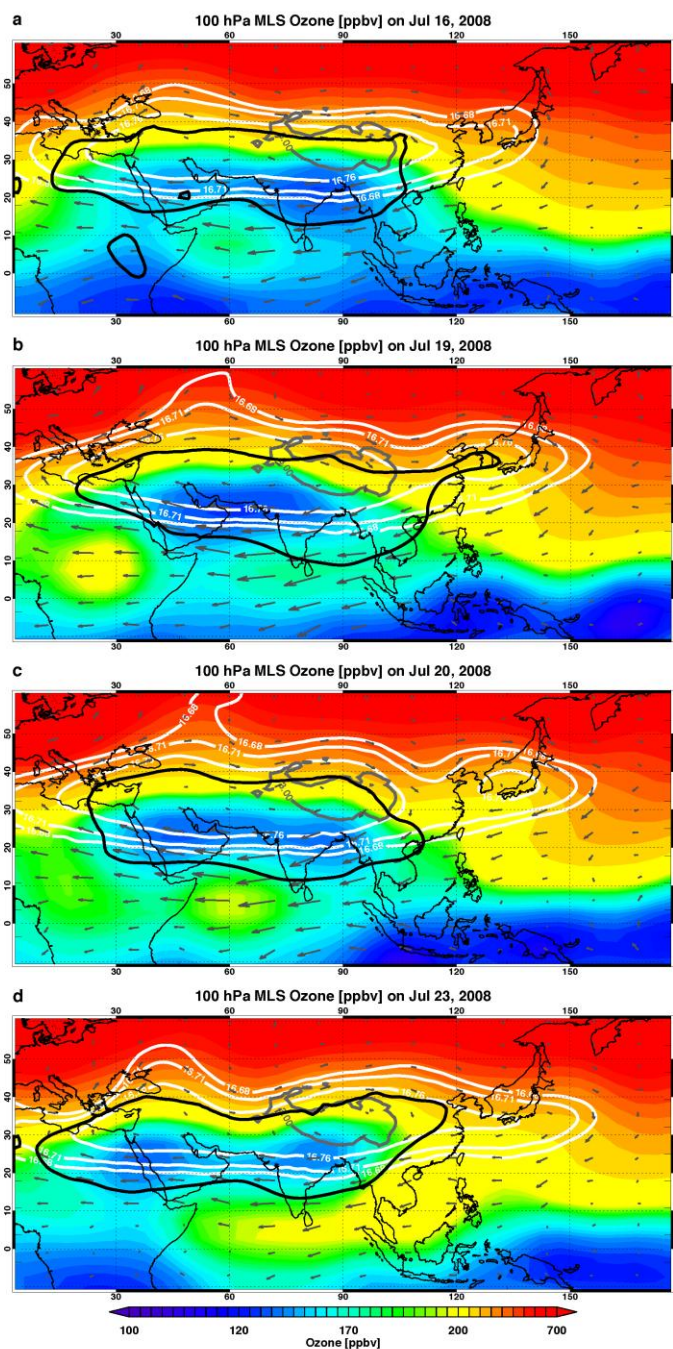


Figure 9: Time series of averaged anomalies over 60-90 °E and 15-35 °N (i.e., the 60-90 ° average of values in Fig.8) for GPH (black line) at 150 hPa, MLS CO (blue line) at 147 hPa, and IASI CO (red line) at 12-16 km from June 1 to August 31 2012. Dash lines represent mean values of each anomaly in the period. The data are smoothed with a 3 day running mean.



5

Figure 10: Daily maps of MLS O_3 mixing ratio at 100 hPa (color shading) on (a) Jul 16, (b) Jul 19, (c) Jul 20, and (d) Jul 23, 2008. The thick gray lines are the 600 hPa contour of surface pressure, indicating the location of the Tibetan Plateau (TP). Gray arrows indicate horizontal wind vectors. The location of the anticyclone is outlined by 100 hPa GPH contours at 16.68, 16.71, and 16.76 km (white) and 105 hPa tropopause (black contour), i.e., the interception of the tropopause with the 105 hPa pressure surface. All values are daily averages; MLS data are mapped using cosine smoothing in $5^\circ \times 5^\circ$ latitude-longitude bins.

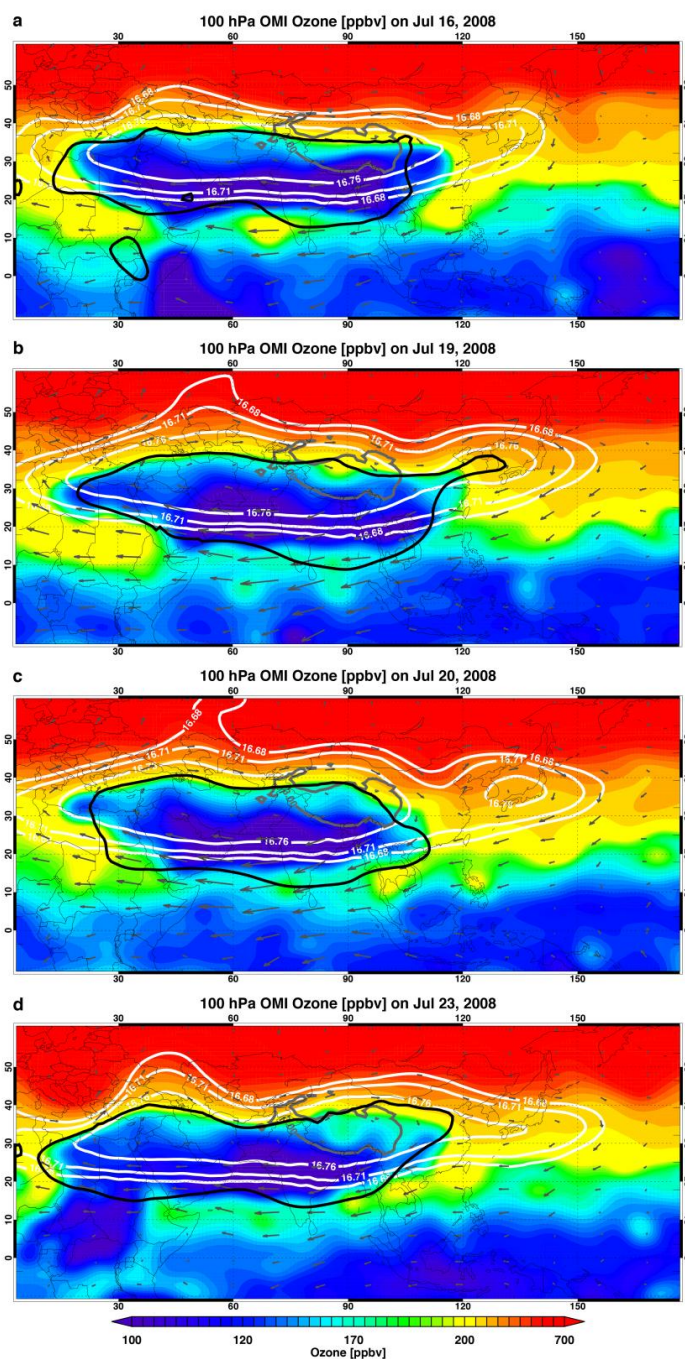


Figure 11: Same as Fig. 10, but for OMI O_3 mixing ratio in layer 18 (approximately 100 hPa). OMI values are mapped in $1^\circ \times 1^\circ$ latitude-longitude grids.

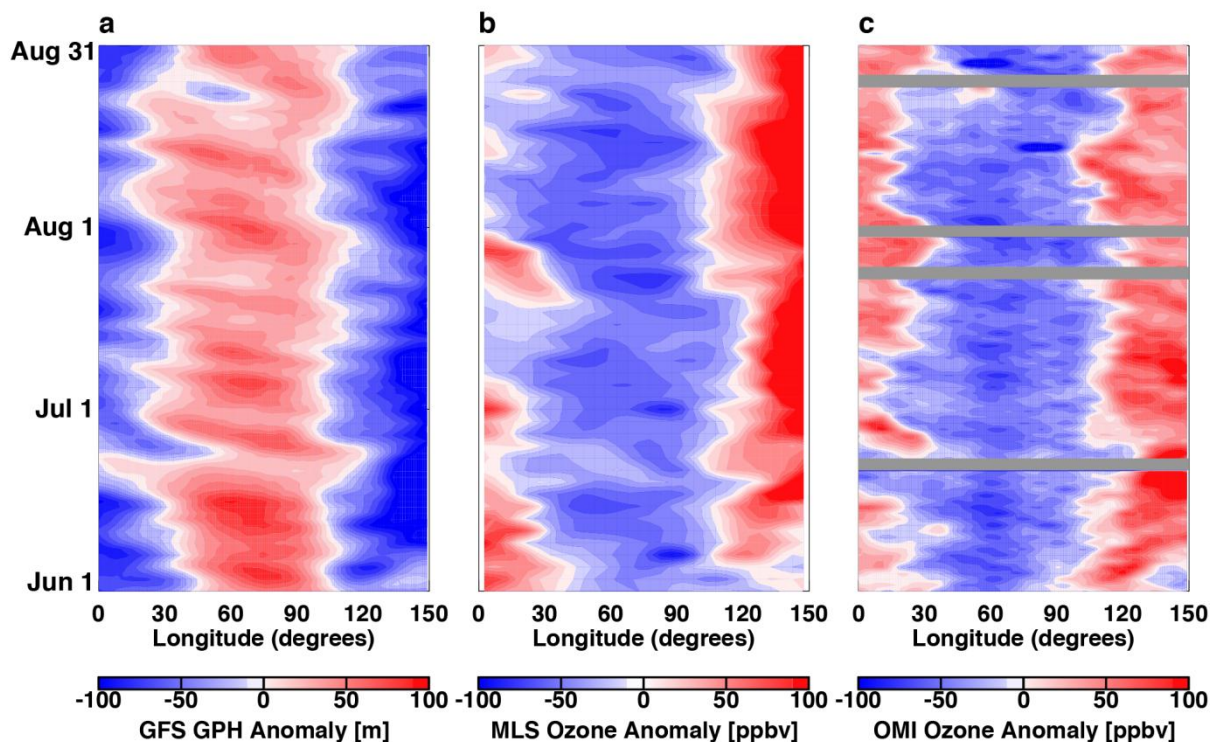


Figure 12: Longitudinal-time (Hovmöller) diagrams for (a) 100 hPa GPH anomalies, (b) 100 hPa MLS O₃ anomalies, and (c) OMI O₃ anomalies at 100 hPa for 2008. Anomalies are calculated with respect to in the regional mean (15–35 °N, 0–150 °E), MLS data has been averaged over 5 ° longitude bins, and OMI data averaged in 1 ° longitude. All the anomalies are daily averaged. Days of missing data are marked in gray.

5

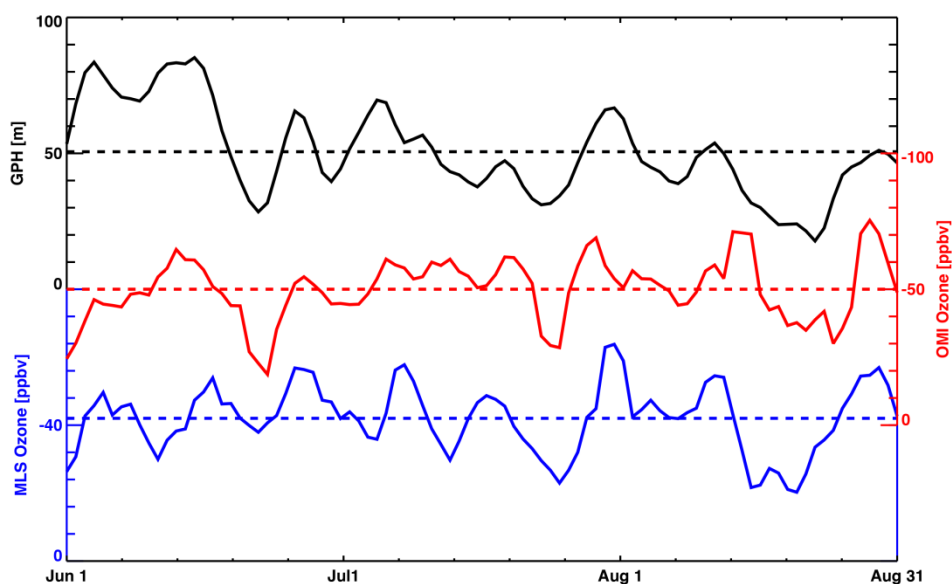


Figure 13: Time series of GPH anomalies (black line), MLS O₃ anomalies (blue line), and OMI O₃ anomalies (red line) at 100 hPa from June 1 to August 31 2008, averaged over 60-90° E and 15-35° N (i.e., the 60-90° average of values in Fig. 12). Dash lines represent mean values of each variable in the period. The data are smoothed using a 3 day running mean.